A Novel CTTC Structure and Optimization Design Method for CLLC Bidirectional Resonant Converter

Min Chen, *Member, IEEE*, Liwen Jia, Bodong Li, Dongbo Zhang, and Feng Jiang

***Abstract*—The resonant tank of CLLC converter incorporates numerous magnetic components. To enhance power density, magnetic integration technology has become a key research focus. This article proposed a new capacitor-transformer-transformer-capacitor (CTTC) structure with variable parameter configuration for the resonant tank of CLLC converter, effectively reducing both the number and volume of magnetic elements. The power transfer characteristics of two magnetic elements at different turns ratio are analyzed, and the design and optimization strategies for the magnetic elements are presented. Compared to the traditional CLLC structure, the proposed CTTC structure effectively reduces volume while maintaining the same control methods and operating modes. The synchronous rectification control method employed by the converter with the proposed CTTC structure is also discussed. A performance evaluation of the CLLC converter utilizing the CTTC structure has been conducted, focusing on the effects of circuit parasitic parameters and leakage inductors. Finally, the validity is verified by a 3 kW bidirectional CLLC prototype.**

***Index Terms*—CLLC bidirectional resonant converter, dual transformer structure, magnetic integration.**

I. INTRODUCTION

WITH the rapid development of electric vehicles, V2G technology has attracted widespread attention [1], [2], which puts forward the need for bidirectional power flow for converters. CLLC bidirectional resonant converter, as shown in Fig. 1, is widely studied due to its full range soft switching characteristics [3], [4], [5], [6], [7], [8], but three magnetic elements in the resonant tank account for a large volume. To solve this problem, magnetic integration technology has been studied.

Magnetic integration can be achieved through the approach of magnetic circuit principle or electrical circuit principle. From the perspective of magnetic circuit integration, given that both the primary and secondary resonant inductors are in series with the transformer, the simplest approach is to utilize the leakage inductor of the transformer as the resonant inductor [9], [10], [11], [12], [13], [14], [15], [16], [17], [18], [19], [20]. However, the magnetic flux of the leakage inductor passes through air, leading to low permeability. This makes the leakage inductor small and difficult to control.

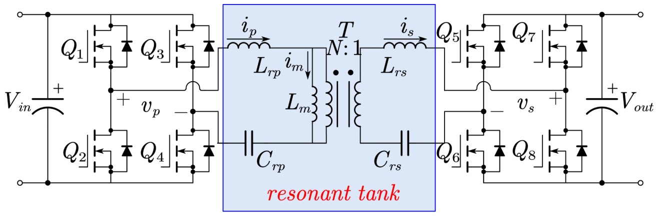

Fig. 1. Schematic diagram of CLLC bidirectional converter.

A common approach to increase the leakage inductor involves widening the gap between the primary and secondary coils. Nevertheless, this approach diminishes the window utilization of magnetic components and simultaneously alters the value of leakage inductor and excitation inductor, making it more challenging to directly calculate the value of inductors and losses [19]. In [13] and [14], finite element simulation software was employed to obtain the value of leakage inductor and losses of planar integrated transformers. However, the process is complex, and the value of leakage inductor is still constrained by the permeability of the surrounding air, rendering it unsuitable as a direct replacement for the resonant inductor. To further increase the value of leakage inductor, one can add additional core material like magnetic shunts [21], [22], [23], [24]. This allows the magnetic flux of the leakage inductor to pass through the magnetic core material rather than through air. However, the use of magnetic shunts can lead to edge effects due to flux around the air gap [24], resulting in increased magnetic losses and additional limitations.

Magnetic circuit integration can also be achieved by altering the shape of the core and the position of the windings, allowing the three magnetic components to be wound on fewer or smaller cores, thereby reducing the volume of the magnetic network [25], [26], [27], [28], [29]. However, since the three magnetic components in the CLLC converter are separate, integrating different magnetic components into a single core by changing the coil winding positions requires precise magnetic circuit design. This involves configuring the relationship between the turns ratio and magnetic reluctance to achieve decoupling [26], [27], [28]. In practical applications, the turns ratio impacts the value of inductor, and magnetic reluctance is related to the core material, both of which impose certain constraints on design and application.

Received 30 August 2024; revised 26 December 2024; accepted 24 January 2025. Date of publication 31 January 2025; date of current version 20 March 2025. Recommended for publication by Associate Editor O. Lucia. *(Corresponding author: Bodong Li.)*

The authors are with the Department of Applied Electronics, Zhejiang University, Hangzhou 310027, China and also with ZJU-Hangzhou Global Scientific and Technological Innovation Center, Hangzhou 311200, China (e-mail: calim@zju.edu.cn; 22310084@zju.edu.cn; bodong_li@zju.edu.cn; 22010073@zju.edu.cn; jiangfeng@zju.edu.cn).

Color versions of one or more figures in this article are available at https://doi.org/10.1109/TPEL.2025.3536010.

Digital Object Identifier 10.1109/TPEL.2025.3536010

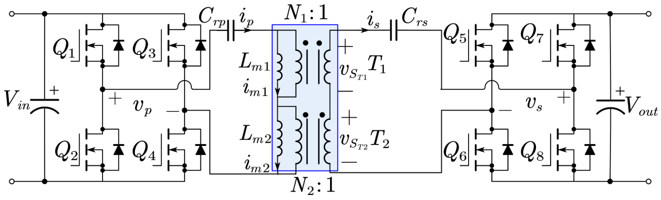

Fig. 2. CLLC converter with proposed CTTC structure.

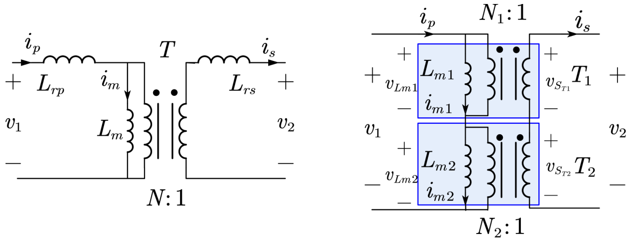

(a) (b)

Fig. 3. Magnetic network. (a) Traditional CLLC structure. (b) CTTC structure.

To sum up, integrating magnetic circuits necessitates tailored designs for magnetic cores and windings, diminishing the universality of magnetic element design. Additionally, the uneven distribution of magnetic flux makes it challenging to calculate and optimize the core losses. Some limitations still exist in practical applications.

From the perspective of electrical circuit principle, changing the network structure of magnetic elements can also reduce the magnetic elements. This approach allows the use of standard magnetic cores, traditional coil winding methods, and loss optimization techniques. In [30], the resonant inductor on secondary side is removed by adjusting the turns ratio and excitation inductor of the transformer. In this approach, the ratio of the excitation inductor to the resonant inductor is determined by the turns ratio of the integrated transformer, limiting its applicability. With only one resonant inductor in series with the resonant capacitor in the resonant tank of the primary sides, the voltage transients caused by the switching actions will superimpose on this inductor, as the voltage across the resonant capacitor remains stable without abrupt changes. This configuration leads to a substantial increase in voltage stress on the inductor. The resonant inductors of the primary and secondary sides can also be integrated into a single magnetic element in the form of coupled inductor through port equivalence [31]. But both structures have inductors, in which the circulating power wastes part of the core volume. In addition, single parameter selection lacks flexibility in use.

In this article, a new capacitor-transformer-transformer-capacitor (CTTC) topology is proposed from the perspective of circuit principles, as shown in Fig. 2. The proposed structure can employ standard cores and windings, avoiding the need for specialized analysis of magnetic and electric fields. In the proposed structure, the elimination of the resonant inductors allows for a reduction in the volume of the magnetic network. The various parameter configurations, such as turns ratio and excitation inductor of the transformers, can be chosen to achieve an equivalent substitution with the traditional CLLC converter. The flexibility in parameter configuration alters the power distribution between the two magnetic elements, enabling the flexible selection of core sizes to avoid redundancy.

The rest of this article is organized as follows. In Section II, the proposed CTTC structure is introduced. The power transmission characteristics and the methods for optimization design of magnetic elements with varying parameters are analyzed in Section III. In Section IV, a synchronous rectification control method applicable to this newly proposed structure is introduced. Additionally, an analysis of the performance of CLLC converter utilizing CTTC structure is conducted, including the effects of parasitic parameters and leakage inductors. In Section V, a 3 kW CLLC converter is designed for experimental verification, and the proposed structure is compared with the traditional CLLC structure to verify its effectiveness. Finally, Section VI concludes this article.

II. CTTC STRUCTURE FOR CLLC CONVERTER

A. Circuit Derivation

Fig. 3(a) shows the magnetic network of traditional CLLC structure, where i_p and i_s are the resonant currents. And the turns ratio, excitation inductor and excitation current of the transformer T are N, L_m, and i_m, respectively.

If the topology of the two magnetic elements is used as the basis without any restrictions on the turns ratio and excitation inductor [31], the new magnetic network can be shown as Fig. 3(b), where the excitation inductor, turns ratio, and excitation current of the magnetic element T_1 are L_{m1}, N_1, and i_{m1}, respectively, and the excitation inductor, turns ratio, and excitation current of the magnetic element T_2 are L_{m2}, N_2, and i_{m2}, respectively. The dotted terminals of T_1 and T_2 are set to be in the same direction. To simplify the analysis, the structural equivalence is initially carried out without considering the leakage inductor of the transformer.

In the new structure, the turns ratio and excitation inductor of the two magnetic elements will be changed. To achieve equivalence, it is necessary to ensure that the voltage and current at the ports remain unchanged when modifying the magnetic network structure. Taking all parameters of T_1 and T_2 as unknown, the port voltages of magnetic network v_1, v_2 can be expressed by port currents of magnetic network i_p, i_s as (1) and (2), respectively, as follows:

$$\begin{cases} v_1 = j\omega L_{rp} i_p + j\omega L_m \left(i_p - \frac{i_s}{N}\right) \\ v_2 = -j\omega L_{rs} i_s + j\omega L_m \frac{1}{N}\left(i_p - \frac{i_s}{N}\right) \end{cases} \tag{1}$$

$$\begin{cases} v_1 = j\omega L_{m1}\left(i_p - \frac{i_s}{N_1}\right) + j\omega L_{m2}\left(i_p - \frac{i_s}{N_2}\right) \\ v_2 = j\omega L_{m1}\frac{1}{N_1}\left(i_p - \frac{i_s}{N_1}\right) + j\omega L_{m2}\frac{1}{N_2}\left(i_p - \frac{i_s}{N_2}\right). \end{cases} \tag{2}$$

Since the values of port voltage v_1 and v_2 are not changed in the equivalence, a system of two equations can be obtained by

TABLE I
PARAMETERS OF TRADITIONAL CONVERTER

Parameters	Values
Input voltage, V_{in}	390 V
Nominal output voltage, V_{out}	260 V
Transformer turn ratio, N	21/14
Excitation inductor, L_m	79.53 μH
Resonant inductor, L_{rp}, L_{rs}	20.93 μH, 9.3 μH
Resonant capacitor, C_{rp}, C_{rs}	100 nF, 225 nF
Resonant frequency, f_r	110 kHz
Switching frequency range	80 kHz–200 kHz

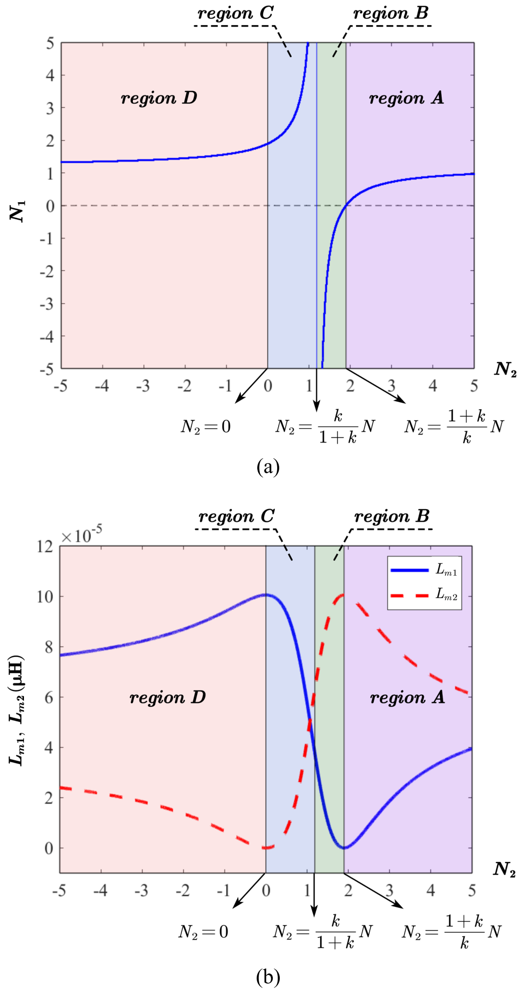

Fig. 4. Change of parameters with N_2. (a) N_1. (b) L_{m1} and L_{m2}.

association

$$\begin{cases} v_1 = j\omega\left(L_{rp}+L_m\right) i_p - j\omega \frac{L_m}{N} i_s \\ \quad = j\omega\left(L_{m1}+L_{m2}\right) i_p - j\omega\left(\frac{L_{m1}}{N_1}+\frac{L_{m2}}{N_2}\right) i_s \\ v_2 = j\omega \frac{L_m}{N} i_p - j\omega\left(L_{rs}+\frac{L_m}{N^2}\right) i_s \\ \quad = j\omega\left(\frac{L_{m1}}{N_1}+\frac{L_{m2}}{N_2}\right) i_p - j\omega\left(\frac{L_{m1}}{N_1^2}+\frac{L_{m2}}{N_2^2}\right) i_s. \end{cases} \tag{3}$$

Also, the values of resonant current i_p and i_s are not changed in the equivalence, it is necessary to ensure that the coefficients in front of the resonant current are equal. That

$$\begin{cases} L_{rp}+L_m = L_{m1}+L_{m2} \\ \frac{L_m}{N} = \frac{L_{m1}}{N_1}+\frac{L_{m2}}{N_2} \\ L_{rs}+\frac{L_m}{N^2} = \frac{L_{m1}}{N_1^2}+\frac{L_{m2}}{N_2^2}. \end{cases} \tag{4}$$

There are four unknown quantities in the new structure: L_{m1}, N_1, L_{m2}, and N_2. However, with only three equations available, there is one degree of freedom for parameter adjustments to achieve structural equivalence, i.e., there is no unique combination of the equivalent parameters. If N_2 is taken as the independent variable, other parameters can be deduced as

$$\begin{cases} N_1 = \frac{N\left[N_2-N\left(1+\frac{1}{k}\right)\right]}{N_2\left(1+\frac{1}{k}\right)-N} \\ L_{m1} = \frac{N_1[(1+k)N-kN_2]}{N(N_1-N_2)} L_{rp} \\ L_{m2} = \frac{N_2[(1+k)N-kN_1]}{N(N_2-N_1)} L_{rp} \end{cases} \tag{5}$$

where $k = L_m/L_{rp}$.

Therefore, there are countless parameter configurations that can achieve equivalent substitutions. The parameter changes with N_2 can be plotted using the data from the 3 kW converter in Table I, as shown in Fig. 4. According to the polarity of N_1 and N_2 in Fig. 4, the whole curve can be divided into four regions and two special value points: A, B, C, D, and the zero and the pole of N_1. The demarcation point of region A and region B is the zero of N_1, and the demarcation point of region B and region C is the pole of N_1.

In region A, with $N_1 > 0$ and $N_2 > 0$, T_1 and T_2 have identical dotted terminals, forming the proposed CTTC structure with series resonant capacitors in the resonant tank, as shown in Fig. 5(a). In region B, with $N_1 < 0$, T_1 is reverse coupled, forming a reverse coupled structure, as shown in Fig. 5(b), which also includes the specific structure proposed in [31]. Since T_1 and T_2 are connected in series in the resonant tank and exhibit symmetry, it can be obtained that regions C and D correspond to the same as regions A and B, respectively. Therefore, subsequent analyses will focus only on regions A and B.

For two specific points, when $N_2 = N(k+1)/k$, $N_1 = 0$, T_1 no longer has an inductive winding on the primary side, but an inductive winding still exists on the secondary side, as shown in Fig. 5(e). When $N_2 = Nk/(k+1)$, $N_1 = \infty$, there is only one inductor exists on the primary side, as shown in Fig. 5(f). This configuration corresponds to the structure proposed in [30].

The structures in the above regions all reduce the number of magnetic components and include the specific structure proposed in [30] and [31]. New structure and variable parameter configuration will bring new magnetic element characteristics. Since the two magnetic components are not coupled with each other, they can be independently designed and analyzed.

III. DESIGN ANALYSIS AND OPTIMIZATION

A. Analysis of Power Transmission Characteristics

The power transmission characteristics of the two magnetic components vary depending on the parameter configuration and need to be analyzed. The fundamental equivalent circuit

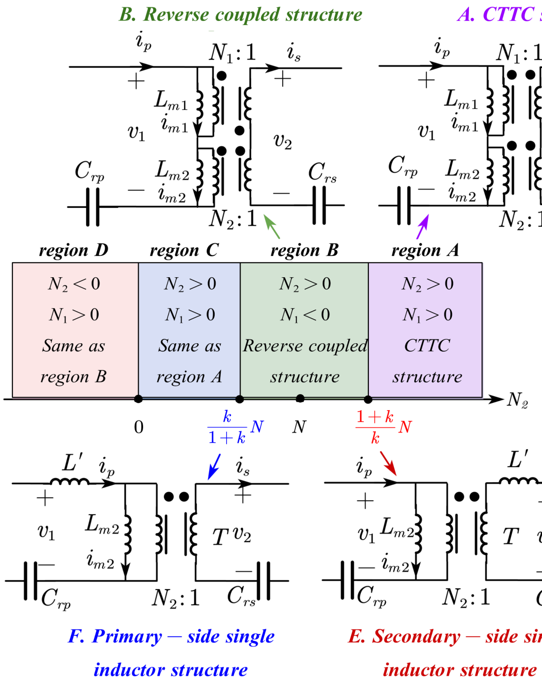

Fig. 5. Variation of magnetic network structure with N_2.

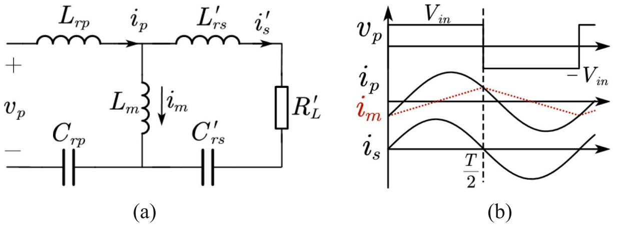

Fig. 6. Traditional CLLC structure. (a) FHA equivalent circuit. (b) Waveforms.

and waveform of the traditional CLLC structure at resonant frequency are shown in Fig. 6, where the secondary side elements are converted to the primary side. $i_s' = i_s/N$, and the rectifier side can be equivalent to a resistor R_L'. i_s is generated by the fundamental component v_{p1} in v_p, and the voltage of L_m can be approximated to v_p, so the current can be expressed as

$$\begin{cases} i_s = N i_s' = N\frac{v_{p1}}{R_L'}\sin(\omega t) = N\frac{4V_{in}}{\pi R_L'}\sin(\omega t) \\ i_p = i_s' + i_m = \frac{v_{p1}}{R_L'}\sin(\omega t) + \frac{V_{in}}{L_m}\left(t-\frac{T}{4}\right) \end{cases} \quad \left(0, \frac{T}{2}\right) \tag{6}$$

where T is the switching cycle of the converter, and $\omega = 2\pi/T$.

The primary and secondary sides of the full-bridge output are square waves symmetrically. Also, the voltage and current in the circuit operate in a half-wave symmetric state. The transmission power can be calculated using half a cycle of the waveform. In Fig. 3(b), v_{ST1} and v_{ST2} are the secondary voltage of T_1 and T_2, and the power transferred by T_1 and T_2 are P_1 and P_2, respectively. They can be calculated as

$$\begin{cases} P_1 = \frac{2}{T}\int_0^{\frac{T}{2}}(v_{ST1} i_s)\,\mathrm{d}t = \frac{2}{T}\int_0^{\frac{T}{2}}\left(\frac{L_{m1}}{N_1}\frac{di_{m1}}{dt} i_s\right)\mathrm{d}t \\ P_2 = \frac{2}{T}\int_0^{\frac{T}{2}}(v_{ST2} i_s)\,\mathrm{d}t = \frac{2}{T}\int_0^{\frac{T}{2}}\left(\frac{L_{m2}}{N_2}\frac{di_{m2}}{dt} i_s\right)\mathrm{d}t \end{cases} \tag{7}$$

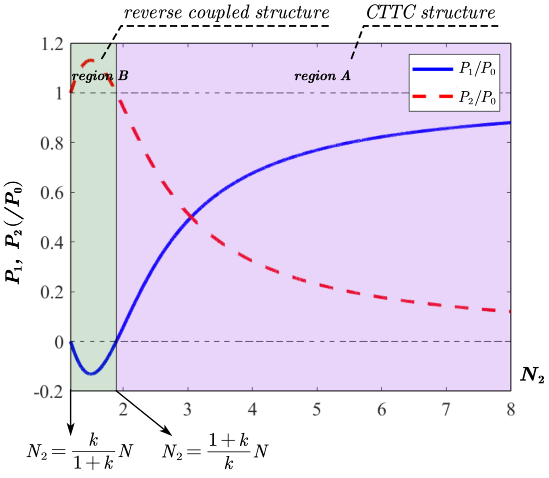

Fig. 7. Power transmission curve of T_1 and T_2.

where $i_{m1} = i_p - i_s/N_1$, $i_{m2} = i_p - i_s/N_2$.

Combining (6) and (7), it can be concluded that

$$\begin{cases} P_1 = \frac{8NL_{m1}V_{in}^2}{\pi^2 N_1 L_m R_L'} \\ P_2 = \frac{8NL_{m2}V_{in}^2}{\pi^2 N_2 L_m R_L'}. \end{cases} \tag{8}$$

By using the rated power P_o as the reference value, the normalized transmission power curve can be plotted, as shown in Fig. 7. It can be conducted that for the reverse coupled structure, T_1 will feed back part of the power to the primary side, then T_2 will transmit an amount greater than the rated power, which wastes part of the core volume. But for the proposed CTTC structure, both T_1 and T_2 transmit power to the secondary side to assume the transformer function. The power transferred by the two magnetic components can be flexibly allocated based on the turns ratio of the two magnetic components. Thus, the size of the entire magnetic network structure can be flexibly selected.

B. Design and Optimization of Magnetic Components

As the transmitted power changes, the size of the magnetic cores will also change. When considering the overall magnetic network, a minimum value for the total volume of magnetic elements emerges. The proposed structure allows for the adjustment of volume distribution between the two magnetic components, enabling a better fit with standard magnetic cores and thereby reducing core redundancy.

Select the magnetic cores based on the AP method [32]. Taking T_1 for instance, when the window area of the transformer is fully utilized, the relationship between the transformer core window area and the winding area can be obtained as follows:

$$\begin{aligned} W_a &= \frac{1}{K_u}(N_p A_{wp} + N_s A_{ws}) \\ &= \frac{1}{K_u}\left(\frac{N_p I_{prms}}{J} + \frac{N_s I_{srms}}{J}\right) \end{aligned} \tag{9}$$

where K_u is window utilization of the core, W_a is window area of magnetic core, N_p and N_s are the respective turns of the primary and secondary windings of T_1, A_{wp} and A_{ws} are the respective conductor cross-sectional areas of the primary and secondary windings, J is the current density, I_{prms} and I_{srms} are the effective values of i_p and i_s, respectively.

According to Faraday's law of electromagnetic induction, the relationship between the induced electromotive force and the magnetic field is as follows:

$$v_p = -N_p \frac{\mathrm{d}\varphi}{\mathrm{d}t} = -N_p A_m \frac{\mathrm{d}B}{\mathrm{d}t} \tag{10}$$

where v_p represents the voltage across the primary winding of T_1, φ is the magnetic flux passing through the primary core, B is the magnetic induction on the primary core, and A_m is the effective cross-sectional area of core.

Because the converter operates periodically, and the waveform of v_p exhibits half-wave symmetry. If t_0 and t_1 are two adjacent zero-crossings in v_p and $v_p > 0$ in (t_0, t_1), then the peak of B is

$$\begin{aligned} B_M &= \frac{1}{2A_m N_p} \int_{t_0}^{t_1} L_{m1} \frac{\mathrm{d}i_{m1}}{\mathrm{d}t} dt \\ &\approx \frac{L_{m1}}{2A_m N_p} \left[i_{m1}(t_1) - i_{m1}(t_0) \right]. \end{aligned} \tag{11}$$

Since $i_{m1}(t_1)$ and $i_{m1}(t_0)$ represent the maximum and minimum values of i_{m1}, respectively, the effective cross-sectional area of the primary core A_m can be expressed as

$$A_m = \frac{L_{m1} i_{m1pk}}{B_M N_p} \tag{12}$$

where $i_{m1pk} = i_{m1}(t_1) = -i_{m1}(t_0)$ is the peak value of i_{m1}.

Then, the AP value of T_1 can be presented as

$$AP_{T1} = W_a A_m = \frac{L_{m1} i_{m1pk}}{K_u B_M J} \left(I_{prms} + \frac{I_{srms}}{N_1} \right). \tag{13}$$

Similarly, the specific value of the AP for T_2 can be calculated. In Section III-A, i_{m1} and i_{m2} have been obtained. Then, the peak value of i_{m1} and i_{m2} under different N_2 conditions can be determined through differential analysis

$$\begin{cases} \frac{di_{m1}}{dt} = \left(1 - \frac{N}{N_1}\right) \omega \frac{v_{p1}}{R'_L} \cos \omega t + \frac{V_{in}}{L_m} \\ \frac{di_{m2}}{dt} = \left(1 - \frac{N}{N_2}\right) \omega \frac{v_{p1}}{R'_L} \cos \omega t + \frac{V_{in}}{L_m} \end{cases} \left(0, \frac{T}{2}\right). \tag{14}$$

Define the peak value of excitation current of T_2 as i_{m2pk}. By discussing the range of N_1 and N_2, the peak value of i_{m1} and i_{m2} within half a cycle under different conditions of N_2 can be obtained, as shown in Table II. The zero-crossing point of di_{m1}/dt and di_{m2}/dt are at t_a and t_b, respectively, as follows:

$$\begin{cases} t_a = \frac{1}{\omega} \arccos\left(\frac{-\pi/4kQ}{1-N/N_1}\right) \\ t_b = \frac{1}{\omega} \arccos\left(\frac{-\pi/4kQ}{1-N/N_2}\right) \\ Q = \sqrt{\frac{L_{rp}}{C_{rp}}} \Big/ R'_L. \end{cases} \tag{15}$$

TABLE II
DISTRIBUTION OF THE MAXIMUM EXCITATION CURRENT

Range of N_2	i_{m1pk}	i_{m2pk}
$\left(\frac{k}{k+1}N, \frac{k+1}{k}N\right)$	$i_{m1}(t_a)$	$i_{m2}\left(\frac{T}{2}\right)$
$\left(\frac{k+1}{k}N, \frac{4kQN}{4kQ-\pi}\right)$	$-i_{m1}(t_a)$	$i_{m2}\left(\frac{T}{2}\right)$
$\left(\frac{4kQN}{4kQ-\pi}, \frac{N(4kQ+k\pi+\pi)}{k(\pi-4Q)}\right)$	$-i_{m1}(t_a)$	$i_{m2}(t_b)$
$\left(\frac{N(4kQ+k\pi+\pi)}{k(\pi-4Q)}, \infty\right)$	$i_{m1}\left(\frac{T}{2}\right)$	$i_{m2}(t_b)$

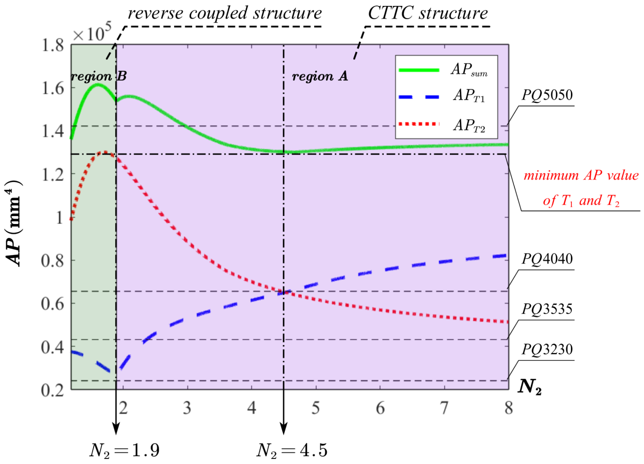

Fig. 8. AP value curve.

The AP values varying with N_2 can be obtained, as shown in Fig. 8. The AP values of the commonly used PQ cores are also shown in Fig. 8. To select a standard magnetic core, several parameter configurations are available. By selecting N_2, the AP values of T_1 and T_2 can both be near the standard cores, the redundancy of the cores can be reduced. The total AP values of the cores is the smallest when $N_2 = 4.5$, and this point is selected for experiment.

IV. CONTROL METHODS AND PERFORMANCE ANALYSIS

A. Synchronous Rectification Strategy

To improve the efficiency, synchronous rectification is needed for the converter. Li et al. [3], Zou et al. [33], and Sankar et al. [34] addressed the issue of synchronous rectification in CLLC converter by theoretically calculating the secondary resonant current of the converter, thereby obtaining the drive signals for synchronous rectification. However, this calculation process is relatively complex. Direct high-frequency detection of the secondary resonant current of the converter, on the other hand, requires higher costs and additional volume [35].

In [4] and [31], a simple and cost-effective voltage detection method has been proposed. But it needs to be modified before it can be applied to the CTTC structure due to the presence of coupling. Since the voltage on the magnetic elements is affected by both i_p and i_s, it is necessary to simultaneously detect the secondary voltage of both to obtain the polar signal

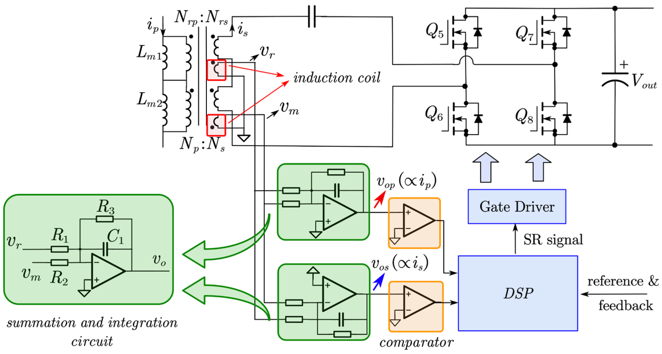

Fig. 9. Synchronous rectification of CTTC structure.

of i_s. The appropriate resonant current detection and rectification schematic is shown in Fig. 9. Two detection coils are wound separately on the cores of T_1 and T_2, with v_r and v_m representing the voltage of the single-turn detection coil. To simplify the integration circuit design, the dotted terminal of the induction coil and the secondary winding of T_1 are wound in the same direction, while those of T_2 are wound in the opposite direction. This configuration enables the restoration of primary and secondary resonant current through the summation and integration circuit. It helps avoid the use of more complex differential integration circuit, reducing detection errors caused by the value inaccuracies of resistor and capacitor also parameter mismatches.

In this detection circuit, the outputs of the two induction coils are

$$\begin{cases} v_r = \dfrac{v_{Lm1}}{N_{rp}} = \dfrac{L_{m1}}{N_{rp}}\dfrac{\mathrm{d}i_p}{\mathrm{d}t} - \dfrac{L_{m1}}{N_1 N_{rp}}\dfrac{\mathrm{d}i_s}{\mathrm{d}t} \\ v_m = -\dfrac{v_{Lm2}}{N_p} = -\dfrac{L_{m2}}{N_p}\dfrac{\mathrm{d}i_p}{\mathrm{d}t} + \dfrac{L_{m2}}{N_2 N_p}\dfrac{\mathrm{d}i_s}{\mathrm{d}t}. \end{cases} \tag{16}$$

And the output of the integration circuit is

$$\begin{aligned} &\frac{v_o}{R_3} + C_1\frac{dv_o}{dt} = -\frac{v_r}{R_1} - \frac{v_m}{R_2} \\ &= \left(\frac{L_{m2}}{R_2 N_p} - \frac{L_{m1}}{R_1 N_{rp}}\right)\frac{\mathrm{d}i_p}{\mathrm{d}t} + \left(\frac{L_{m1}}{R_1 N_1 N_{rp}} - \frac{L_{m2}}{R_2 N_2 N_p}\right)\frac{\mathrm{d}i_s}{\mathrm{d}t}. \end{aligned} \tag{17}$$

According to (17), the output voltage v_o is related to both primary resonant current i_p and secondary resonant current i_s. To solve the coupling problem, i_p and i_s can be obtained by scaling the calculations based on v_r and v_m.

If $L_{m2}/(R_2 C_1 N_p) = L_{m1}/(R_1 C_1 N_{rp}) = k_1$, component of i_p can be removed that

$$\frac{v_{os}}{R_3 C_1} + \frac{\mathrm{d}v_{os}}{\mathrm{d}t} = \left(\frac{1}{N_1} - \frac{1}{N_2}\right) k_1 \frac{\mathrm{d}i_s}{\mathrm{d}t}. \tag{18}$$

While if $L_{m1}/(R_1 C_1 N_1 N_{rp}) = L_{m2}/(R_2 C_1 N_2 N_p) = k_2$, i_s can be removed that

$$\frac{v_{op}}{R_3 C_1} + \frac{\mathrm{d}v_{op}}{\mathrm{d}t} = (N_2 - N_1)\, k_2 \frac{\mathrm{d}i_p}{\mathrm{d}t}. \tag{19}$$

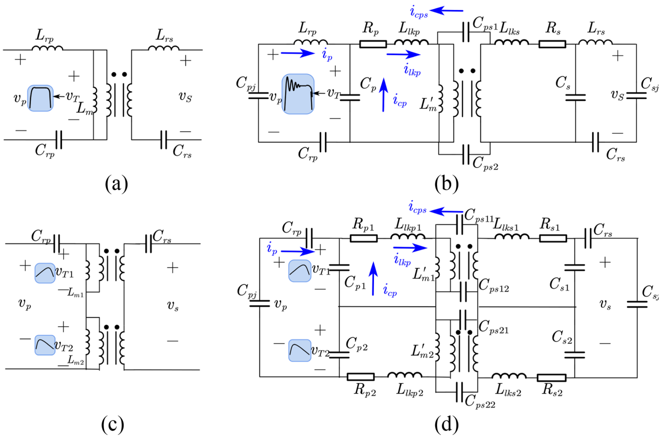

Fig. 10. Resonant network of CLLC converter. (a) Basic model of traditional CLLC structure. (b) Parasitic model of traditional CLLC structure. (c) Basic model of CTTC structure. (d) Parasitic model of CTTC structure.

TABLE III
MEASURED TRANSFORMER PARAMETERS

Transformer	T of CLLC structure	T_1 of CTTC structure	T_2 of CTTC structure
L_m(μH)	80.836	37.45	65.82
L_{lkp}(μH)	5.64	0.815	5.43
L_{lks}(μH)	2.55	0.96	0.17
C_p(pF)	47.294	64.068	24.921
C_s(pF)	38.278	90.213	98.961
C_{ps1}(pF)	95.783	173.094	111.790
C_{ps2}(pF)	95.564	172.972	112.091
R_p(mΩ)	121.78	71.18	135.40
R_s(mΩ)	83.85	78.85	34.79

After integration, the polar signals of i_p and i_s can be obtained by the comparator, which are captured by the controller to generate the drive signal for synchronous rectification.

B. Parasitic Effects Analysis

In practical CLLC circuits, various parasitic parameters can cause oscillations and must be accounted for in applications.

Generally, a commonly used transformer model contains four stray capacitors, including winding capacitors C_p and C_s, stray capacitors between primary and secondary windings C_{ps1} and C_{ps2} [36], [37], [38]. L_{lkp}, L_{lks}, R_p, and R_s are leakage inductors and resistors of transformer. C_{pj} and C_{sj} are the equivalent junction capacitors of MOSFETs. The resonant network of traditional CLLC converter and CTTC structure with and without parasitic elements are depicted in Fig. 10.

In ideal conditions, the voltage V_T across the transformer approximates a square wave. Due to the presence of stray capacitors, the chopper voltage of full bridge, parasitic capacitors, and resonant inductors form a voltage loop. The parasitic capacitors will resonate with inductors to generate high-frequency oscillations, causing a peak voltage on V_T. Through MAXWELL simulations and measurements, the values of parasitic capacitors are shown in Table III.

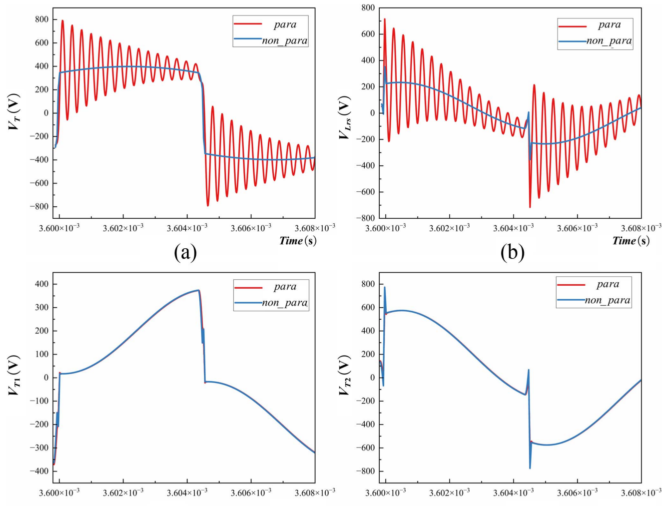

(a) (b) (c) (d)

Fig. 11. Voltage waveform of the magnetic component as the interlayer capacitance varies. (a) V_T in traditional CLLC structure. (b) V_{Lrs} in traditional CLLC structure. (c) V_{T1} in CTTC structure. (d) V_{T2} in CTTC structure.

Fig. 11(a) and (b), respectively, show the simulation waveforms of V_T and V_{Lrs} in the traditional CLLC structure, with and without considering the parasitic parameters of transformer. After incorporating parasitic parameters into the simulation, voltage oscillations with a frequency of approximately 10^6 Hz still appeared on the waveforms even when the damping effect was taken into account. The frequency of voltage oscillations can be theoretically estimated using (20), which aligns with simulation results. In CTTC structure, the voltage loop still exists. However, the large value of resonant capacitors provides a clamping effect, effectively suppressing high-frequency oscillations on the terminal voltage of transformer in CTTC structure. Fig. 11(c) and (d), respectively, show the simulation waveforms of V_{T1} and V_{T2} in CTTC structure. It can be observed that the waveforms of V_{T1} and V_{T2} do not exhibit significant changes before and after considering the parasitic parameters, indicating that the presence of parasitic parameters does not substantially cause voltage oscillations

$$\begin{cases} f_{\text{oscillation}} = \frac{1}{2\pi\sqrt{L_1 C_1}} \\ L_1 \approx L_{rp}\,(\text{or } L_{rs}) \\ C_1 \approx C_p||\mathrm{C}_{pj}||\mathrm{C}_{rp}\,(\text{or} C_s||\mathrm{C}_{sj}||\mathrm{C}_{rs})\,. \end{cases} \tag{20}$$

Based on the preceding analysis, the CTTC structure can avoid high-frequency voltage oscillations on the magnetic components due to the clamping effect of resonant capacitors and the elimination of resonant inductors. The reduction of voltage oscillations in CTTC structure not only lowers circuit noise but also helps to reduce losses in the magnetic components to some extent.

C. Leakage Effects Analysis

The generation of leakage inductors is inevitable during the design of transformers. In CTTC structure, the leakage inductor generated by the transformers will simultaneously affect key parameters such as the equivalent turns ratio, resonant inductor, and excitation inductor. Therefore, the sensitivity of these key parameters to leakage inductor is analyzed to ensure equivalent reliability.

As shown in Fig. 10(d), after considering leakage inductors, the theoretical values L_{m1}, L_{m2} and actual values L'_{m1}, L'_{m2} of the excitation inductors have the following relationship:

$$\begin{cases} L_{m1} = L'_{m1} + L_{lkp1} \\ L_{m2} = L'_{m2} + L_{lkp2} \end{cases} \tag{21}$$

where L_{lkp1} and L_{lkp2} represent the primary leakage inductor of T_1 and T_2, respectively.

In Section II-A, the equivalence of magnetic element parameters between the two structures is derived from traditional CLLC structure based on (4) and represented in (5). Similarly, the inverse solution of (5) provides magnetic element parameters in traditional CLLC converter based on those in CTTC structure. For analytical simplicity, assuming symmetry in the parameters of traditional CLLC structure, it can be concluded that the parameters in traditional CLLC structure are

$$\begin{cases} N'_{lk} = \sqrt{\left(L'_{m1} + L'_{m2}\right) \Big/ \left(\frac{L'_{m1}}{N_1^2} + \frac{L'_{m2}}{N_2^2}\right)} \\ L'_{m\_lk} = N'_{lk}\left(\frac{L'_{m2}}{N_2} + \frac{L'_{m1}}{N_1}\right) \\ L'_{rp\_lk} = L'_{m1} + L'_{m2} - L'_{m\_lk} + L_{lkp1} + L_{lkp2} \end{cases} \tag{22}$$

where $N'_{lk}, L'_{m\_lk}, L'_{rp\_lk}$ are the turns ratio of transformer, excitation inductor, and primary inductor of traditional CLLC structure expressed in terms of the component parameters in CTTC structure, taking leakage inductor into account, respectively.

Since leakage inductor directly affects excitation inductor in transformer manufacturing, an analysis is conducted on how variations in excitation inductor, influenced by leakage inductor, impact key parameters

$$\begin{cases} \Delta N = \frac{N_1^2 N_2^2\left(N_1^2 - N_2^2\right)}{2N\left(L_{m1}N_2^2 + L_{m2}N_1^2\right)^2}\left(L_{m2}\Delta L_{m1} - L_{m1}\Delta L_{m2}\right) \\ \Delta L_m = \left(\frac{L_{m2}\left(N_1^2 - N_2^2\right)}{2N\left(L_{m1}N_2^2 + L_{m2}N_1^2\right)} + \frac{N}{N_1}\right)\Delta L_{m1} \\ \qquad - \left(\frac{L_{m1}\left(N_1^2 - N_2^2\right)}{2N\left(L_{m1}N_2^2 + L_{m2}N_1^2\right)} - \frac{N}{N_2}\right)\Delta L_{m2} \\ \Delta L_{rp} = -\Delta L_m. \end{cases} \tag{23}$$

According to (23), the parameter sensitivity of key parameters in traditional CLLC structure versus excitation inductors in CTTC structure is shown in Fig. 12. As leakage inductor affects the performance of transformer, the leakage inductor of good high-frequency transformers is often kept within 5%. In Fig. 12, the maximum variation for the equivalent turns ratio is 2.8%. For the equivalent excitation inductor and resonant inductor, the maximum variation is 5%. Notably, the effects of the leakage inductors from the two transformers in CTTC structure can cancel each other out for all the key parameters, further ensuring equivalent reliability.

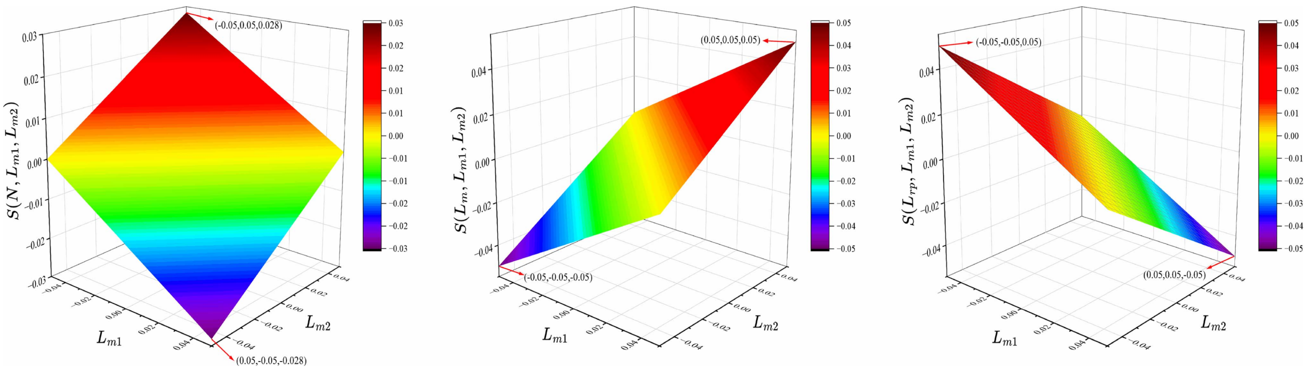

(a) (b) (c)

Fig. 12. Sensitivity of the key parameters with respect to L_{m1} and L_{m2}. (a) N. (b) L_m. (c) L_{rp}.

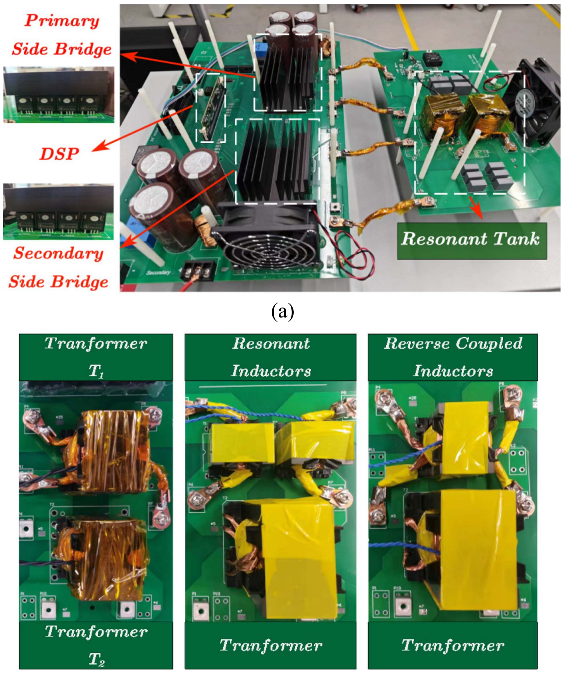

(a)

(b) (c) (d)

Fig. 13. CLLC prototype. (a) CLLC converter. (b) CTTC structure. (c) Traditional CLLC structure. (d) Reverse coupled structure.

Overall, by appropriately adjusting the leakage inductor of the two transformers, the impact on the key parameters is minor and within a reasonable range. According to the traditional analysis of CLLC converter, when the key parameters are unchanged, the voltage gain range, switching frequency range, and other performance characteristics of the converter will also remain consistent, allowing for the equivalence of different structures.

V. EXPERIMENTAL VERIFICATION

A 3 kW CLLC prototype is built for comparison and verification. The prototype, CTTC structure, traditional CLLC structure, and reverse coupled structure are shown in Fig. 13. To provide the control signal, a TMS320F28335 Digital Signal Processor is implemented. Switches are SiC MOSFET of IMZA65R048M1H. The parameters of CTTC structure and reverse coupled structure are shown in Table IV, which is equivalent to the parameters of traditional CLLC structure in Table I. All magnetic elements use PC95 series PQ cores.

TABLE IV
CONVERTER PARAMETERS

Structure	Parameters	Values
Reverse coupled structure [31]	L_{m1}, L_{m2}	10.46μH, 90μH
	N_1, N_2	-12/8, 21/14
CTTC structure	L_{m1}, L_{m2}	36.18μH, 64.28μH
	N_1, N_2	14/15, 27/6

TABLE V
MAGNETIC PARAMETERS

Structure	Magnetic core	Total effective volume	Total area
Traditional CLLC structure	PQ5050+PQ3230*2	61200mm^3	3008mm^2
Reverse coupled structure [31]	PQ5050+PQ3535	54500mm^3	2510mm^2
CTTC structure	PQ4040*2	41000mm^3	2240mm^2

Table V shows the total volume and area of the magnetic cores used in the three magnetic network structures. Compared to traditional CLLC structure, the volume of the magnetic network in CTTC structure has been reduced by 33%. Additionally, in comparison to reverse coupled structure, both magnetic components in CTTC structure transfer power to the secondary side with minimal circulation, further reducing the core volume by 24.8%.

Fig. 14 shows the waveforms of the CTTC structure at the turn-ON moment, where i_p is the primary resonant current, V_{GS4} and V_{DS} are the driving signal and drain source voltage of Q_4. Fig. 14(a), (b), and (c) shows the waveforms of the converter operating in the below-resonant-frequency mode (BRFM) ($f_s < f_r$), resonant-frequency mode (RFM) ($f_s = f_r$), and above-resonant-frequency mode (ARFM) ($f_s > f_r$), respectively. The V_{GS} of the MOSFET will be enabled only after the V_{DS} of the

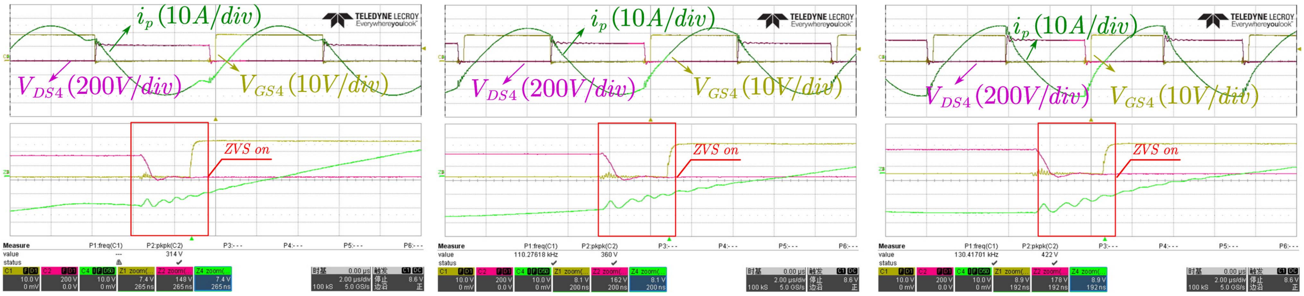

(a) (b) (c)

Fig. 14. Waveforms of CTTC structure at the moment of turn-ON. (a) Below-resonant-frequency mode (BRFM) ($f_s < f_r$). (b) Resonant-frequency mode (RFM) ($f_s = f_r$). (c) Above-resonant-frequency mode ($f_s > f_r$).

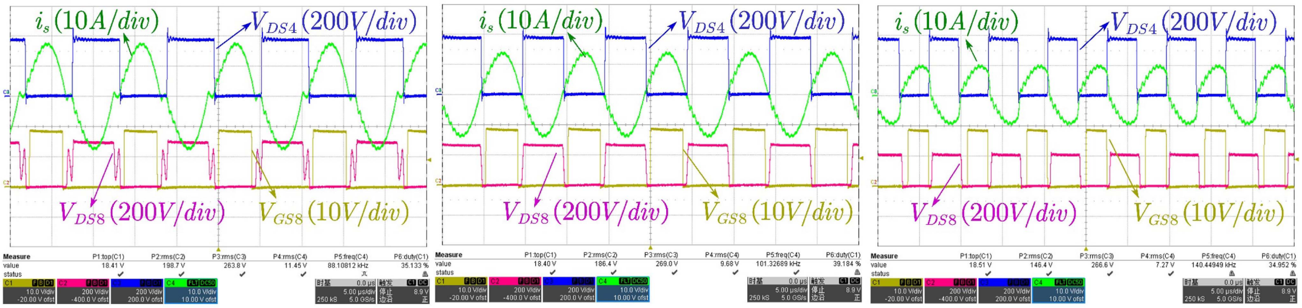

(a) (b) (c)

Fig. 15. Forward operating waveforms in traditional CLLC structure. (a) $V_{\text{out}} = 300$ V (BRFM). (b) $V_{\text{out}} = 260$ V (RFM). (c) $V_{\text{out}} = 200$ V (ARFM).

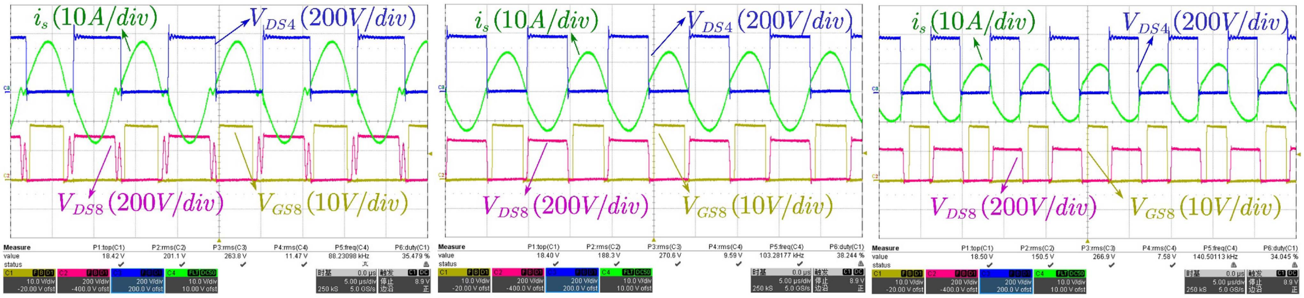

(a) (b) (c)

Fig. 16. Forward operating waveforms in reverse coupled structure. (a) $V_{\text{out}} = 300$ V (BRFM). (b) $V_{\text{out}} = 260$ V (RFM). (c) $V_{\text{out}} = 200$ V (ARFM).

MOSFET drops to 0, indicating that CTTC structure has ZVS at all operating frequencies.

The forward operating waveforms of traditional CLLC structure with $V_{\text{out}} = 300$ V, 260 V, and 200 V are shown in Fig. 15(a)–(c), where i_s is the secondary resonant current, V_{DS4} is the drain source voltage of Q_4, V_{GS8}, and V_{DS8} are the synchronous rectification driving signal and drain source voltage of Q_8, respectively. The input voltages are 390 V. When the output voltage of the converter is 300 V, 260 V, and 200 V, the operating frequencies of the converter are 90 kHz, 110 kHz, and 140 kHz respectively. That is, the converter operates in BRFM, RFM, and ARFM, respectively. The forward operating waveforms of the reverse coupled structure and the CTTC structure under the same gain are shown in Figs. 16(a)–(c) and 17(a)–(c).

Experimental results in Figs. 15–17 show that all structures can achieve proper synchronous rectification control, verifying the practicality of the synchronous rectification method. The converter with three different resonant tank exhibits essentially identical voltage, current, and other operating waveforms in the BRFM, RFM, and ARFM, indicating that equivalent substitution has been achieved. Similarly, the CLLC converter with three different magnetic network structures can exhibit similar operating characteristics at the same operating frequency when the converter is operated in backward mode. The detailed experimental

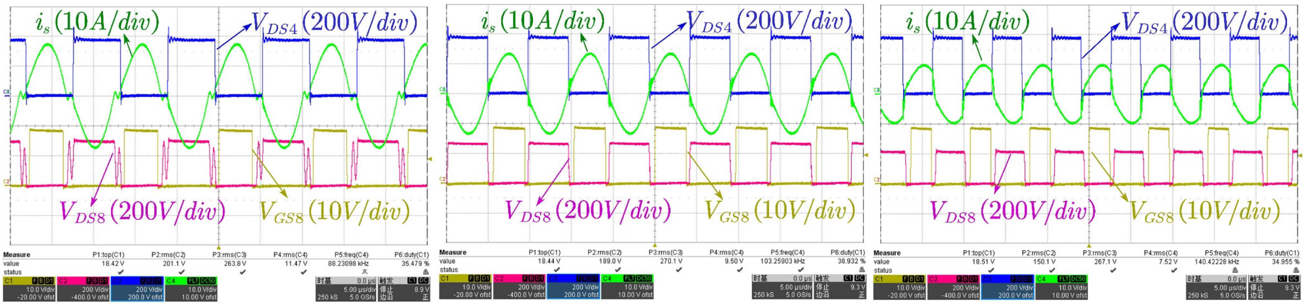

(a) (b) (c)

Fig. 17. Forward operating waveforms in CTTC structure. (a) $V_{\text{out}} = 300$ V (BRFM). (b) $V_{\text{out}} = 260$ V (RFM). (c) $V_{\text{out}} = 200$ V (ARFM).

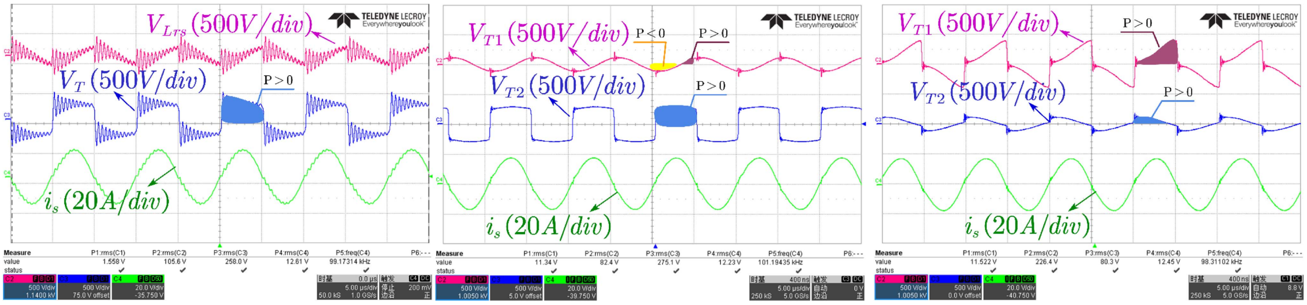

(a) (b) (c)

Fig. 18. Voltage and current waveforms of magnetic components. (a) Traditional CLLC structure. (b) Reverse coupled structure. (c) CTTC structure.

waveforms of backward mode, along with the corresponding verification results, are provided in the appendix for validation.

Fig. 18 illustrates the operating voltage of the magnetic elements and resonant current waveforms in the three structures. Specially, V_{Lrs} and V_T are the voltage of the secondary resonant inductor and the secondary side of transformer in traditional CLLC structure, respectively, V_{T1} and V_{T2} are the voltage of the secondary side of the two transformers in reverse coupled structure and CTTC structure, respectively. Consistent with the theoretical analysis and simulation results, in traditional CLLC structure, high-frequency oscillations of the order of 10^6 Hz in frequency appear on the voltage waveforms of the magnetic element despite the existence of system damping. However, in the proposed structure, the voltage waveforms of the magnetic components have almost no high-frequency oscillations, significantly reducing circuit noise.

Moreover, according to the phase relationship between current and voltage, $P > 0$ indicates that the power is transmitted to secondary side, whereas $P > 0$ indicates transmission to primary side. In CTTC structure, as shown in Fig. 18(c), both T_1 and T_2 transmit power to the secondary side with minimal circulation. In contrast, the reverse coupled structure has T_2 functioning as a traditional transformer, transmitting power only to the secondary side, while T_1 acts as an inductor with substantial circulating power. Because the magnetic network after equivalence does not alter the resonant current. This implies a consistent requirement for conductor diameter in the primary and secondary windings. The presence of circulating currents and feedback power to the primary side leads to higher average and effective voltages across the magnetic components when the converter transmits equal power. Given the same core cross-sectional areas, this leads to increased peaks in magnetic induction intensity. Thus, compared to the CTTC structure, which transmits only active power to the secondary side, the reverse coupled structure necessitates larger magnetic components to reduce magnetic flux density peaks, as shown in Table V.

Observing the resonant current waveforms of the three structures above reveals slight oscillation differences. Since there is no series inductor in CTTC structure, the current can easily experience abrupt changes during the uncontrolled dead time. As shown in Fig. 10(d), when the converter switches from Q_1 and Q_4 being ON to Q_2 and Q_3 being ON, C_{p1} and C_{p2} generate a displacement current i_{cp} due to the voltage interruption, which reduces primary resonant current i_p momentarily, thereby reducing the turn-OFF loss of primary switches. The current reduction will also superimpose oscillations due to the presence of parasitic inductor on the line. While in the traditional CLLC structure, the larger resonant inductors impede the sudden current change, so the resonant current waveform does not show significant variation when the switch is turned OFF. Fig. 19(a)–(c), respectively, present the waveforms of three structures. The phenomena shown in Fig. 19 are consistent with the theoretical analysis. In the CTTC structure, the i_p will decrease to some extent due to oscillation during the dead time, which can reduce

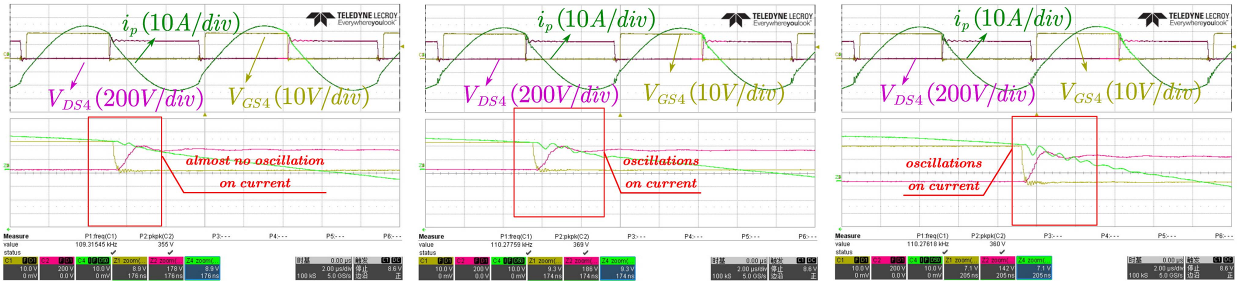

(a) (b) (c)

Fig. 19. Waveforms at the moment of turn-OFF. (a) Traditional CLLC structure. (b) Reverse coupled structure. (c) CTTC structure.

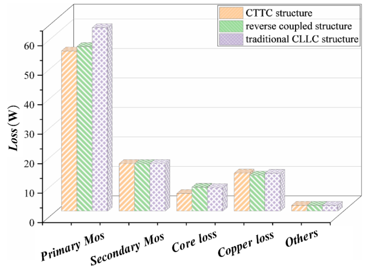

Fig. 20. Loss analysis of converters with three different structures.

the turn-OFF loss of the converter. Moreover, this oscillation will not impair the normal operation of the converter.

Fig. 20 illustrates the loss distribution of the converter with three different structures when operating at the resonant frequency under rated power conditions. According to theoretical analysis, in the proposed structure where there is no resonant inductor, the parasitic capacitors of magnetic component cause the resonant current to momentarily decrease during dead time, thereby reducing turn-OFF losses. Due to the different parameters in CTTC structure and reverse coupled structure, the reduction in turn-OFF losses slightly varies between them. For the switches in the secondary side, all three structures use a similar synchronous rectification control method, resulting in comparable losses. Regarding magnetic component losses, the CTTC structure reduces circulating current compared to the reverse coupled structure, thereby reducing core losses. The copper losses of the magnetic components are nearly identical across the three structures.

The efficiency of the traditional CLLC structure, the reverse coupled structure, and the proposed CTTC structure at various output powers is shown in Fig. 21. The efficiency test points are set at the resonant frequency. The output power increases as the load resistance decreases and the efficiency is measured by YOKOGAWA WT500. In forward operation, the proposed CTTC structure achieves a maximum efficiency of 97.01%, which is 0.44% higher than the peak efficiency of the traditional CLLC structure. In backward operation, the proposed CTTC structure achieves a maximum efficiency of 96.99%, which is 0.18% higher than the peak efficiency of the traditional CLLC structure. Additionally, although the CTTC structure reduces circulating current compared to the reverse coupled structure, the overall efficiency only improves slightly due to the

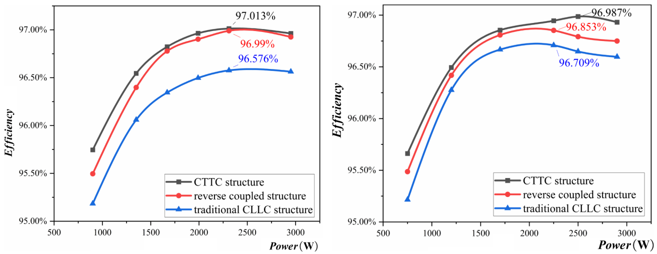

(a) (b)

Fig. 21. Efficiency comparison curves of three different structures at different power. (a) Forward mode. (b) Backward mode.

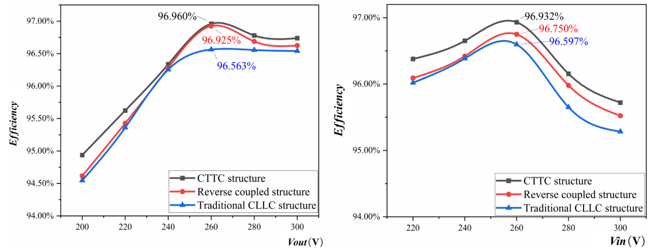

(a) (b)

Fig. 22. Full-load efficiency comparison curves of three different structures at different voltages. (a) Forward mode. (b) Backward mode.

significant reduction in core volume. Meanwhile, as there will be application scenarios where the voltage of dc bus is constant while the battery voltage fluctuates when the CLLC converter is applied in V2G, Fig. 22 presents the operating efficiency of the converter under such application scenarios. The output power is set at 3 kW. In the forward mode, the input voltages of the converter remain unchanged. By varying the operating frequency of the converter, different output voltages are obtained, thereby yielding the curve shown in Fig. 22(a). In the backward mode, the input voltages of the converter are different. Through adjusting the operating frequency to make the output power the same, the curve presented in Fig. 22(b) is obtained. As previously discussed, the proposed CTTC structure improves efficiency without changing the control method and operational characteristics.

VI. CONCLUSION

To reduce the volume of the CLLC converter, this article proposes a novel CTTC structure, offering an equivalent

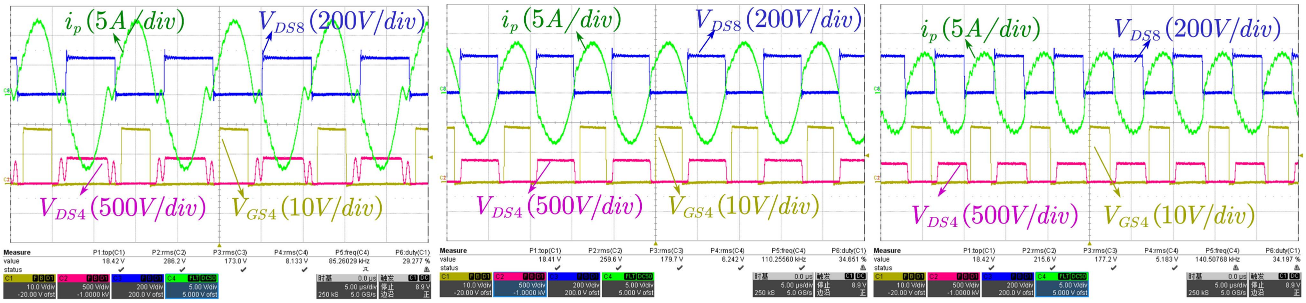

(a) (b) (c)

Fig. 23. Backward operating waveforms in traditional CLLC structure. (a) $V_{\text{out}} = 410$ V (BRFM). (b) $V_{\text{out}} = 390$ V (RFM). (c) $V_{\text{out}} = 330$ V (ARFM).

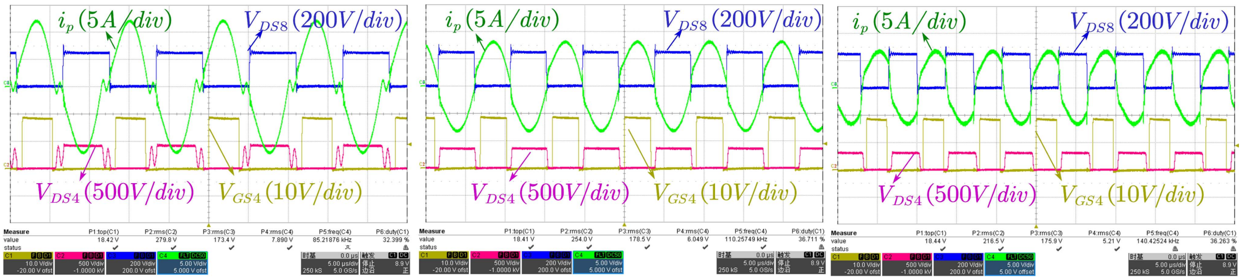

(a) (b) (c)

Fig. 24. Backward operating waveforms in reverse coupled structure. (a) $V_{\text{out}} = 410$ V (BRFM). (b) $V_{\text{out}} = 390$ V (RFM). (c) $V_{\text{out}} = 330$ V (ARFM).

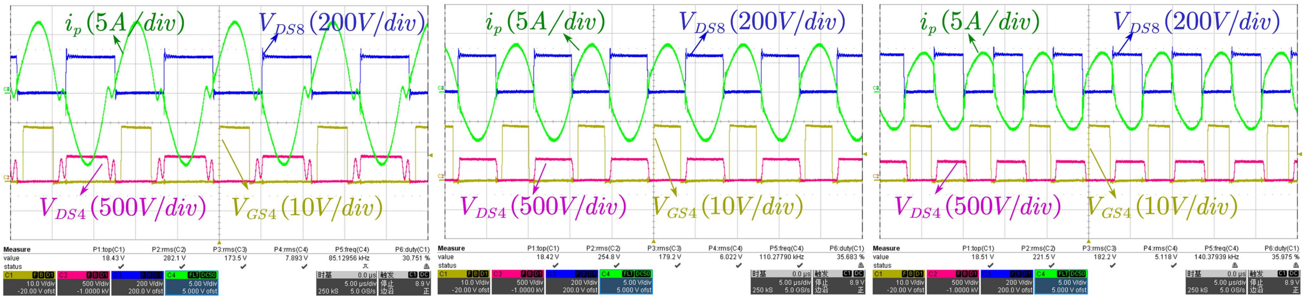

(a) (b) (c)

Fig. 25. Backward operating waveforms in CTTC structure. (a) $V_{\text{out}} = 410$ V (BRFM). (b) $V_{\text{out}} = 390$ V (RFM). (c) $V_{\text{out}} = 330$ V (ARFM).

alternative to the traditional CLLC converter. The advantages of employing the CTTC structure in a CLLC converter are as follows:

1) the ability to employ various parameter configurations to achieve equivalence with the traditional CLLC converter;
2) flexible adjustment of power distribution among magnetic components to use standard cores and minimize the overall volume of magnetic elements;
3) no need for complex magnetic circuit design and control methods, and the operating modes of the converter are basically unchanged;
4) the presence of circuit parasitic parameters does not impair the normal operation of the converter;
5) improvement of the efficiency of converter without changing the control mode.

Finally, a 3 kW prototype was used for experimental verification. Without affecting the operational mode of the converter, the total volume of the CTTC structure is reduced by 33% compared to the traditional CLLC structure and by 24.8% compared to the reverse coupled structure, effectively reducing the size of the magnetic network structure. Furthermore, the proposed CTTC structure is a structurally universal equivalent method, not limited to the configuration of magnetic components, and can be combined with other magnetic integration methods to further reduce the volume of the magnetic network.

APPENDIX

The backward operating waveforms of traditional CLLC structure with $V_{\text{out}} = 410$ V, 390 V, and 330 V are shown in

Fig. 23(a)–(c), where i_p is the primary resonant current, V_{DS8} is the drain source voltage of Q_8, V_{GS4} and V_{DS4} are the synchronous rectification driving signal and drain source voltage of Q_4, respectively. In Fig. 23(a)–(c), the operating frequencies of the converter are 85 kHz, 110 kHz, and 140 kHz, respectively. That is, the converter operates in BRFM, RFM, and ARFM, respectively. The backward operating waveforms of the reverse coupled structure and CTTC structure under the same voltage gain are shown in Figs. 24(a)–(c) and 25(a)–(c). It is evident that the proposed rectification strategy operates effectively, and the synchronous rectification drive provides accurate results. Also, the experimental results demonstrate that CLLC converters with three different magnetic network structures can achieve the same operating characteristics and the range of voltage gain as well.

ACKNOWLEDGMENT

The authors would like to thank ZJU-PLEXIM Joint Simulation Laboratory for the support of the powerful simulation tools PLECS and also like to thank the Microgrid Electrical Equipment and Manufacture Platform in the Polytechnic Institute of Zhejiang University, on which many valuable tests in this article were performed.

REFERENCES

[1] X. Wang, M. Chen, B. Li, and N. Chen, “Multifunction control strategy for single-phase AC/DC power conversion systems with voltage-sensorless power-decoupling function,” *IEEE Trans. Power Electron.*, vol. 35, no. 12, pp. 13602–13620, Dec. 2020.

[2] W. Zhang and J. Wang, “Research on V2G control of smart microgrid,” in *Proc. Int. Conf. Comput. Eng. Intell. Control*, Nov. 2020, pp. 216–219.

[3] B. Li, M. Chen, X. Wang, N. Chen, X. Sun, and D. Zhang, “An optimized digital synchronous rectification scheme based on time-domain model of resonant CLLC circuit,” *IEEE Trans. Power Electron.*, vol. 36, no. 9, pp. 10933–10948, Sep. 2021.

[4] N. Chen et al., “Synchronous rectification based on resonant inductor voltage for CLLC bidirectional converter,” *IEEE Trans. Power Electron*, vol. 37, no. 1, pp. 547–561, Jan. 2022.

[5] B. Li, M. Chen, X. Sun, J. Wang, and F. Jiang, “A hybrid control for smooth power direction transition of bidirectional resonant CLLC converter with wide voltage gain,” *IEEE Trans. Power Electron.*, vol. 39, no. 12, pp. 15898–15914, Dec. 2024, doi: 10.1109/TPEL.2024.3448375.

[6] W. Chen, P. Rong, and Z. Lu, “Snubberless bidirectional DC–DC converter with new CLLC resonant tank featuring minimized switching loss,” *IEEE Trans. Ind. Electron.*, vol. 57, no. 9, pp. 3075–3086, Sep. 2010.

[7] Z. Zhang, C. Liu, M. Wang, Y. Si, Y. Liu, and Q. Lei, “High-efficiency high-power-density CLLC resonant converter with low-stray-capacitance and well-heat-dissipated planar transformer for EV on-board charger,” *IEEE Trans. Power Electron.*, vol. 35, no. 10, pp. 10831–10851, Oct. 2020.

[8] J.-H. Jung, H.-S. Kim, M.-H. Ryu, and J.-W. Baek, “Design methodology of bidirectional CLLC resonant converter for high-frequency isolation of DC distribution systems,” *IEEE Trans. Power Electron.*, vol. 28, no. 4, pp. 1741–1755, Apr. 2013.

[9] A. Kats, G. Ivensky, and S. Ben-Yaakov, “Application of integrated magnetics in resonant converters,” in *Proc. IEEE Appl. Power Electron. Conf.*, 1997, vol. 2, pp. 925–930.

[10] G. Liu, D. Li, Y. Jang, and J. Zhang, “Over 300 kHz GaN device based resonant bidirectional DCDC converter with integrated magnetics,” in *Proc. IEEE Appl. Power Electron. Conf. Expo.*, 2016, pp. 595–600.

[11] H. Wang, S. An, T. Chang, and Q. Ma, “Design and optimization of magnetically integrated planar transformer based on bi-directional CLLC resonant converter,” in *Proc. IEEE Int. Power Electron. Appl. Conf. Expo.*, 2022, pp. 1120–1123.

[12] A. Soni and A. K. Dhakar, “Bi-directional CLLC resonant converter with integrated planar transformer for energy storage systems,” in *Proc. IEEE 46th Annu. Conf. Ind. Electron. Soc.*, 2020, pp. 4255–4260.

[13] P. He, A. Mallik, G. Cooke, and A. Khaligh, “High-power-density high-efficiency LLC converter with an adjustable-leakage-inductance planar transformer for data centers,” *IET Power Electron.*, vol. 12, no. 2, pp. 303–310, Feb. 2019.

[14] P. He, A. Mallik, A. Sankar, and A. Khaligh, “Design of a 1-MHz high-efficiency high-power-density bidirectional GaN-based CLLC converter for electric vehicles,” *IEEE Trans. Veh. Technol.*, vol. 68, no. 1, pp. 213–223, Jan. 2019.

[15] C. W. Park and S. K. Han, “Design of an integrated magnetics structure for LLC resonant converter,” in *Proc. 43rd Annu. Conf. IEEE Ind. Electron. Soc.*, Oct./Nov. 2017, pp. 1888–1893.

[16] A. Chandwani and A. Mallik, “Parametric modeling and characterization of leakage-integrated planar transformer for CLLC DC–DC converter,” *IEEE Trans. Magn.*, vol. 58, no. 6, Jun. 2022, Art. no. 8600308.

[17] J. Biela and J. W. Kolar, “Electromagnetic integration of high power resonant circuits comprising high leakage inductance transformers,” in *Proc. IEEE 35th Annu. Power Electron. Specialists Conf.*, 2004, pp. 4537–4545.

[18] D.-N. Nguyen, T.-T. Pham, T.-N. Quang, and D.-D. Nguyen, “Design of a planar transformer for bidirectional resonant type converters in on-board charger applications: A methodological approach,” in *Proc. IEEE 10th Int. Conf. Commun. Electron.*, 2024, pp. 678–683.

[19] G. Liu, D. Li, J. Q. Zhang, B. Hu, and M. L. Jia, “Bidirectional CLLC resonant DC-DC converter with integrated magnetic for OBCM application,” in *Proc. IEEE Int. Conf. Ind. Technol.*, 2015, pp. 946–951.

[20] S. Zou, J. Lu, A. Mallik, and A. Khaligh, “Modeling and optimization of an integrated transformer for electric vehicle on-board charger applications,” *IEEE Trans. Transp. Electrific.*, vol. 4, no. 2, pp. 355–363, Jun. 2018.

[21] S. A. Ansari, J. N. Davidson, and M. P. Foster, “Fully-integrated transformer with asymmetric primary and secondary leakage inductances for a bidirectional resonant converter,” *IEEE Trans. Ind. Appl.*, vol. 59, no. 3, pp. 3674–3685, May/Jun. 2023.

[22] M. Li, Z. Ouyang, and M. A. E. Andersen, “High-frequency LLC resonant converter with magnetic shunt integrated planar transformer,” *IEEE Trans. Power Electron.*, vol. 34, no. 3, pp. 2405–2415, Mar. 2019.

[23] J. Zhang, Z. Ouyang, M. C. Duffy, M. A. E. Andersen, and W. G. Hurley, “Leakage inductance calculation for planar transformers with a magnetic shunt,” *IEEE Trans. Ind. Appl.*, vol. 50, no. 6, pp. 4107–4112, Nov./Dec. 2014.

[24] D. Bündgen, A. Thönnessen, and R. W. De Doncker, “Integration of high leakage inductance transformers utilizing genetically optimized curved foil windings,” in *Proc. 11th Int. Conf. Power Electron.*, 2023, pp. 316–322.

[25] J. Yang, Y. Xu, X. Wu, and F. Muhammad, “High density planar integrated magnetics with two-sided merged inductor windings and integrated cores for resonant DC/DC converter,” *IEEE J. Emerg. Sel. Topics Power Electron.*, vol. 12, no. 1, pp. 195–207, Feb. 2024.

[26] S. Gao and Z. Zhao, “Magnetic integrated LLC resonant converter based on independent inductance winding,” *IEEE Access*, vol. 9, pp. 660–672, 2021.

[27] M. Noah et al., “A current sharing method utilizing single balancing transformer for a multiphase LLC resonant converter with integrated magnetics,” *IEEE J. Emerg. Sel. Topics Power Electron.*, vol. 6, no. 2, pp. 977–992, Jun. 2018.

[28] W. Martinez et al., “Three-phase LLC resonant converter with integrated magnetics,” in *Proc. IEEE Energy Convers. Congr. Expo.*, Sep. 2016, pp. 1–8.

[29] B. Li, Q. Li, and F. C. Lee, “High-frequency PCB winding transformer with integrated inductors for bi-directional resonant converter,” *IEEE Trans. Power Electron.*, vol. 34, no. 7, pp. 6123–6135, Jul. 2019.

[30] Z. U. Zahid, Z. M. Dalala, R. Chen, B. Chen, and J.-S. Lai, “Design of bidirectional DC–DC resonant converter for vehicle-to-grid (V2G) applications,” *IEEE Trans. Transport. Electrific.*, vol. 1, no. 3, pp. 232–244, Oct. 2015.

[31] M. Chen et al., “A coupled inductor scheme for CLLC bidirectional converter and optimized current detection method,” *IEEE Trans. Power Electron.*, vol. 37, no. 10, pp. 11546–11551, Oct. 2022.

[32] C. W. T. McLyman, *Transformer and Inductor Design Handbook*, 3rd ed. New York, NY, USA: Marcel Dekker, 2004.

[33] S. Zou, J. Lu, A. Mallik, and A. Khaligh, “Bi-directional CLLC converter with synchronous rectification for plug-in electric vehicles,” *IEEE Trans. Ind. Appl.*, vol. 54, no. 2, pp. 998–1005, Mar./Apr. 2018.

[34] A. Sankar, A. Mallik, and A. Khaligh, “Extended harmonics based phase tracking for synchronous rectification in CLLC converters,” *IEEE Trans. Ind. Electron.*, vol. 66, no. 8, pp. 6592–6603, Aug. 2019.

[35] G. K. Y. Ho, R. Yu, and B. M. H. Pong, “Current driven synchronous rectifier with saturable current transformer and dynamic gate voltage control for LLC resonant converter,” in *Proc. IEEE Appl. Power Electron. Conf. Expo.*, 2012, pp. 2345–2351.

[36] M. A. Saket, M. Ordonez, M. Craciun, and C. Botting, “Improving planar transformers for LLC resonant converters: Paired layers interleaving,” *IEEE Trans. Power Electron.*, vol. 34, no. 12, pp. 11813–11832, Dec. 2019.

[37] F. Blache, J.-P. Keradec, and B. Cogitore, “Stray capacitances of two winding transformers: Equivalent circuit measurements calculation and lowering,” in *Proc. IEEE Ind. Appl. Soc. Annu. Meeting*, 1994, vol. 2, pp. 1211–1217.

[38] L. Dalessandro, F. da Silveira Cavalcante, and J. W. Kolar, “Self-capacitance of high-voltage transformers,” *IEEE Trans. Power Electron.*, vol. 22, no. 5, pp. 2081–2092, Sep. 2007.

Min Chen (Member, IEEE) received the B.S. degree in applied electronics and the Ph.D. degree in electrical engineering from Zhejiang University, Hangzhou, China, in 2000 and 2006, respectively.

From 2007 to 2009, he was a Postdoctoral Researcher with the Department of Electrical Engineering, Zhejiang University. From 2010 to 2014, he was a Lecturer, and in 2014 was promoted as an Associate Professor. Since 2020, he has been a Full Professor with Zhejiang University. From 2014 to 2015, he was a Visiting Researcher with the Department of Energy Technology, Aalborg University. He has authored or coauthored more than 80 SCI/EI-indexed papers and was issued for almost 30 patents of inventions. He is currently the Director of ZJU Joint Research Center for New Energy and Power Electronics Based Power System and the Deputy Director of the National Engineering Research Center for Applied Power Electronics. His research interests include application of power electronics in power system, inverter and its control, renewable energy generation and grid connection, and bidirectional energy conversion technology for electric vehicle energy storage and charging.

Liwen Jia received the B.S. degree in electrical engineering from Zhejiang University, Hangzhou, China, in 2023. She is currently working toward the M.S. degree in electrical engineering with the College of Electrical Engineering, Zhejiang University, Hangzhou, China.

Her research interests include bidirectional dc–dc resonant converters and optimal design of magnetic components.

Bodong Li received the B.S. degree in electrical engineering from Yanshan University, Qinhuangdao, China, in 2016, and the M.S. and Ph.D. degrees in electrical engineering from Zhejiang University, Hangzhou, China, in 2020 and 2024, respectively.

He is currently a Postdoctoral Researcher with the Department of Electrical Engineering, Zhejiang University. His research interests include high efficiency dc–dc converters, energy storage systems, photovoltaic, and microgrid systems.

Dongbo Zhang received the B.S. degree in electrical engineering from Zhejiang University, Hangzhou, China, in 2020, and the M.S. degree in electrical engineering from the College of Electrical Engineering, Zhejiang University, Hangzhou, China, in 2023.

His research interests include wireless power transmission and high efficiency converters for renewable energy.

Feng Jiang was born in Anhui Province, China. He received the M.S. degree in electrical engineering from Zhejiang University, Hangzhou, China, in 2019.

He is an Assistant Researcher with the College of Electrical Engineering, Zhejiang University. His research interests include microgrid controller, application of power electronics in power system and renewable energy.